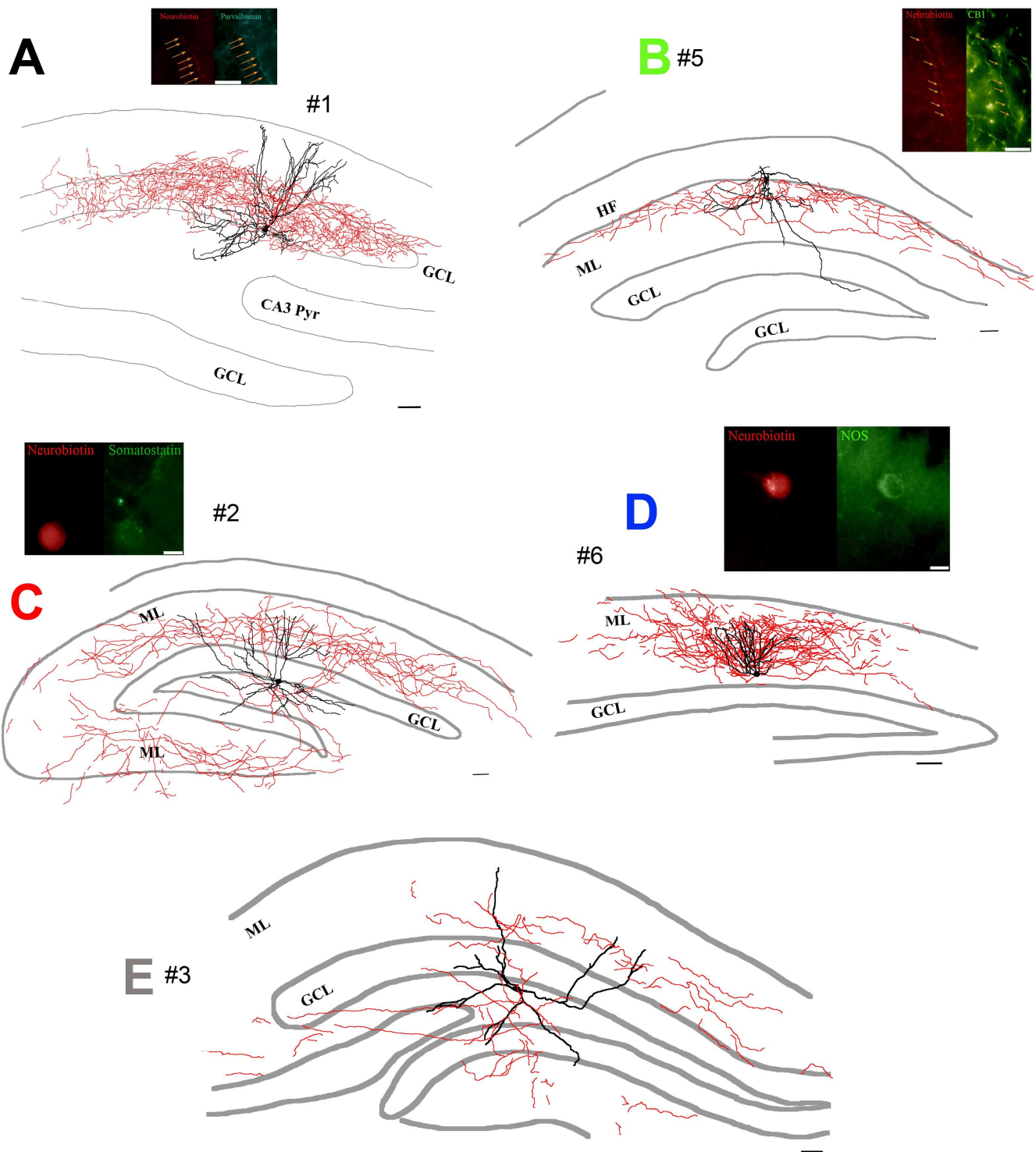**Supplemental Information**

# Intrinsic interneurons



**Figure S1 (Related to Figure 1). Examples of intrinsic interneurons (DG$_{INT}$). (A)** Fast-spiking-basket cell (same as in Figure 2A) 2D reconstruction and immunopositivity for parvalbumin. Arrows indicate PV positive boutons. For clarity, in all panels in this figure, axons from three consecutive, 60µm thick sections are shown, together with all the dendrites. **(B)** Reconstruction of an interneuron located in the molecular layer (ML) and projecting to the outer molecular layer of the DG. Arrows indicate cannabinoid type 1 receptor positive boutons. **(C)** Total molecular layer (TML; Hosp et al., Hippocampus, 2014) innervating cell (same as in Figure 2B) and somatostatin (SOM) immunopositivity. **(D)** Molecular layer perforant path associated cell (MOPP) and its immunopositivity for nitrogen monoxide synthase (NOS). **(E)** Reconstruction of a neurochemically not identified interneuron located in the hilus and innervating the inner half of the molecular layer. For all cells, red intenotes axons and black dendrites and somas. Color scheme for panel labels A-E are as in Fig 3E: black: PV, red: SOM, green: CB1: blue: NOS; grey: not tested. Scale bars: 50µm for the reconstructions, 10µm for images. GCL: granule cell layer; ML: molecular layer; pyr: pyramidal layer; HF: hippocampal fissure.
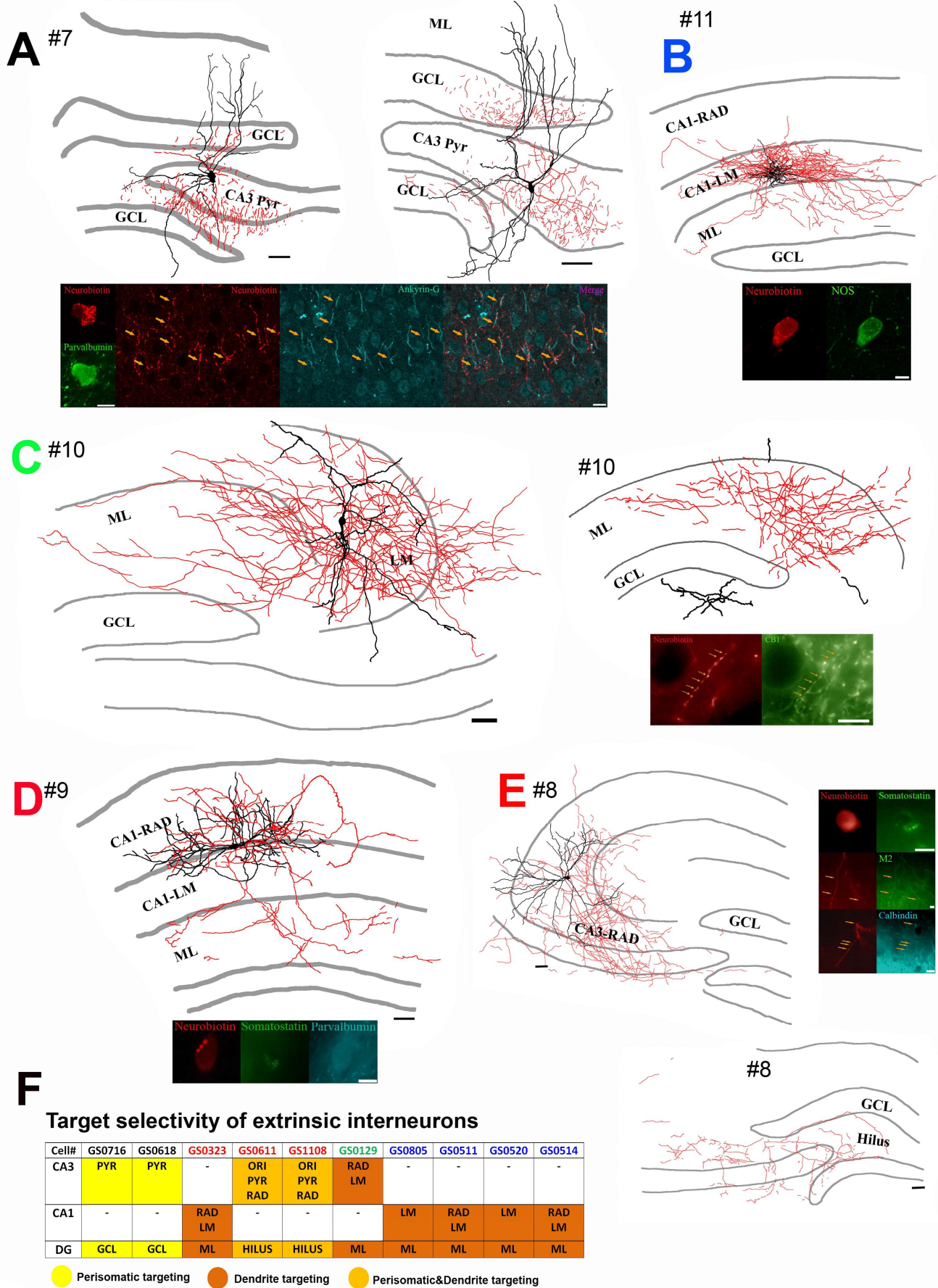
# Extrinsic interneurons



**A** #7

ML
GCL
GCL
CA3 Pyr
GCL
GCL
CA3 Pyr
GCL

Neurobiotin — Neurobiotin — Ankyrin-G — Merge
Parvalbumin

**B** #11

CA1-RAD
CA1-LM
ML
GCL

Neurobiotin — NOS

**C** #10

ML
GCL
LM

#10
ML
GCL

Neurobiotin — CB1

**D** #9

CA1-RAD
CA1-LM
ML

Neurobiotin — Somatostatin — Parvalbumin

**E** #8

CA1-RAD
CA3-RAD
GCL

Neurobiotin — Somatostatin
M2
Calbindin

#8
GCL
Hilus

**F**

## Target selectivity of extrinsic interneurons

| Cell# | GS0716 | GS0618 | GS0323 | GS0611 | GS1108 | GS0129 | GS0805 | GS0511 | GS0520 | GS0514 |
|---|---|---|---|---|---|---|---|---|---|---|
| CA3 | PYR | PYR | - | ORI PYR RAD | ORI PYR RAD | RAD LM | - | - | - | - |
| CA1 | - | - | RAD LM | - | - | - | LM | RAD LM | LM | RAD LM |
| DG | GCL | GCL | ML | HILUS | HILUS | ML | ML | ML | ML | ML |

🟡 Perisomatic targeting  🟠 Dendrite targeting  🟠 Perisomatic&Dendrite targeting

**Figure S2 (Related to Figure 1). Examples of extrinsic interneurons (DG$_{EXT}$)**

**Figure S2.** (legend continued)

(**A**) Reconstructions of two CA3 axo-axonic cells innervating the two blades of the DGs, in addition to the CA3 pyramidal layer (cell on the right is the same one as in Figure 3A). For clarity, axons (red) from three consecutive, 60μm thick sections are shown, together with all the dendrites (black). Bottom: confocal image showing PV immunopositivity of cell on the left and its axons targeting Ankyrin-G-decorated axon initial segments (arrows). (**B**) CA1 neurogliaform cell with axons crossing the hippocampal fissure and innervating the molecular layer of the DG. For clarity, axons (red) from four consecutive, 60μm thick sections are shown, together with all the dendrites (black). Confocal image depicts NOS immunopositivity. (**C**) Left: reconstruction of a perforant path associated (PPA)-like cell (Lasztoczi et al., Journal of Neuroscience, 2011; same as in Figure 3C) located in the CA3 and innervating the molecular layer; for clarity, only four 60μm thick consecutive sections are shown. Right: reconstruction of three consecutive sections corresponding to the same cell starting at ~90μm from the soma. In this portion of the cell, the majority of the axons (red) targeted the molecular layer of the DG. Below: immunopositivity for CB1 receptor (arrows). (**D**) Reconstruction of a CA1 interneuron (same as in Figure 3B) whose axons (red) cross the hippocampal fissure and penetrate into the molecular layer of DG; inset: corresponding fluorescent image depicting immunopositivity for SOM and PV. (**E**) Reconstruction of a CA3 cell (left) that projects to the hilus (bottom). Upper drawing depicts all the dendrites (black) as well as axons (red) from three consecutive sections for clarity. Bottom drawing shows axons of two consecutive sections starting at ~330μm from the soma. Confocal images on the right indicate SOM immunopositivity of the soma, muscarinic acetylcholine receptor type 2 (M2) and calbindin immunopositivity of the dendrites (arrows). (**F**) Summary of the dendritic or somatic layer specificity of the axonal projections for the DG$_{EXT}$ cells in the CA1/3 and the DG. Color scheme for panel labels A-E are as in Fig 3E: black: PV, red: SOM, green: CB1: blue: NOS. Scale bars: 50μm for the reconstructions, 10μm for images. GCL: granule cell layer; ML: molecular layer; pyr: pyramidal layer; HF: hippocampal fissure; RAD: stratum radiatum; LM: stratum lacunosum-moleculare.
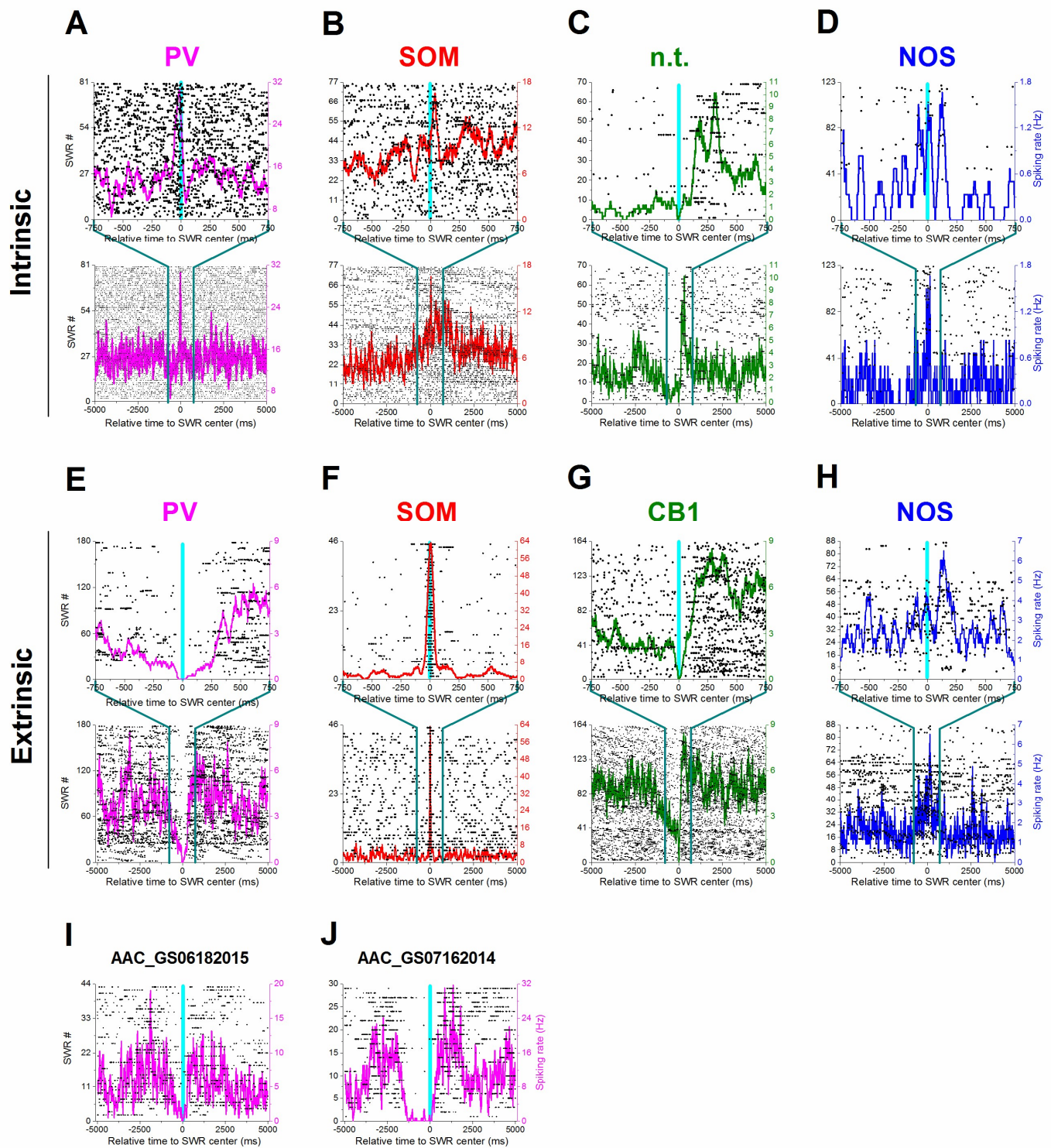
**Figure S3 (Related to Figure 4). Additional examples of the temporal dynamics of SWR-dependent modulation of DG$_{INT}$ and DG$_{EXT}$ interneuronal firing, illustrated at two time scales.** (A-D) Example raster plots (black dots) and spiking rate curves (in color) showing spiking patterns for 3 neurochemically labeled DG$_{INT}$ and one neurochemically unidentified DG$_{INT}$ cell type. Upper row: 1.5s wide time window; lower row: 10s wide time window. (**A**) Fast spiking basket cell. (**B**) TML cell (same as in S1C.) (**C**) Hilar cell, same as in S1E; n.t.: neurochemical identity not tested. Note that the peak firing rate is shifted to the right following the strong reduction at SWR center. (**D**) MOPP-cell, same as in S1D. Vertical cyan line depicts SWR center. (**E-H**) Similar to A-D but for four neurochemically labeled extrinsic cell types. (**E**) CA3 axo-axonic cell (cell on the right in S2A). Note the decrease in firing long preceding SWR. (**F**) Hilar-projecting CA3 cell, same as in S2E. (**G**) PPA cell (same as in Figure 3C and in S2C). Note the early modulation and the right-shifted peak firing rate following the strong reduction in firing at SWR center. (**H**) Another example of a neurogliaform cell (morphology not shown) with a right-shifted peak firing with respect to the SWR center. (**I-J**) Raster plots and spiking rate curves for two axo-axonic cells (Figs S3E and 4E) when only solitary SWRs were considered, i.e., when data for SWRs co-occurring within a 5000 ms long window (I), or 2500 ms (D), were rejected.

**Supplemental Experimental Procedures**


**Animals**

All animals were housed in a vivarium under a constant 12hr light/dark cycle with access to food and water ad libitum. Mice were kept on cages of 1-5 animals/cage, rats were singly housed in individual cages.

**Viral production and intrahippocampal injections**

Briefly, P7 male pups were anesthetized on ice and placed on an ice cold neonatal rat stereotaxic adapter (Stoelting, Wood Dale, IL) in a Kopf stereotaxic frame (Tujunga, CA). Bilateral burr holes were drilled into the skull and 1 μL of Syn-GTR was injected at a rate of 0.1 μL/min using a 5 μL Hamilton syringe with the following coordinates (in mm from bregma and mm below the skull): caudal 2.0, lateral 1.5, depth 2.7.

At P112-126, RbV-mCh viral stocks were diluted 500-fold to avoid non-specific labeling and injected bilaterally into the dorsal dentate gyrus to trace monosynaptic inputs onto Syn-GTR infected, neonatally-born DGCs. Animals were anesthetized using a Ketamine/Xylazine mixture. RbV-mCh (2 μL) was injected at a rate of 0.1 μL/min at the following coordinates (in mm from bregma and mm below the skull): caudal 4.2, lateral 2.3, depth 4.2.

**Juxtacellular recordings and related surgical procedures**

Recordings were started approximately 30 mins after the termination of anesthesia, when the animal became completely alert. Two borosilicate recording electrodes at 15° from the vertical plane were lowered into the brain, one was placed into the CA1 str. pyramidale (LFP channel, positioned where the SWR amplitude was the highest), and the other (juxtacellular pipette) was used for the unit recording in the hippocampus proper and in the DG. Juxtacellular recordings and field recordings were performed using an ELC-03XS universal amplifier (NPI Electronics) and a Neurodata IR283 (Cygnus Technology) amplifier, respectively. The LFP electrode was filled with 1M NaCl solution, juxtacellular electrode was filled with 0.5M NaCl or Ringer solution containing 135mM NaCl, 5.4mM KCl, 5mM HEPES, 1.8mM $CaCl_2$, and 1mM $MgCl_2$ (pH was adjusted to 7.2 by adding NaOH; target osmolality was 290mmol). The juxtacellular electrode (12-20 MΩ) also contained 1.5-2% (wt/vol) Neurobiotin tracer (SP1120; Vector Laboratories) or biotin-ethylenediamine (N-(2-Aminoethyl)Biotinamide, HBr) (A1593; Thermofisher Scientific) as a tracer for juxtacellular labelling. Both channels were low pass (Bessel) filtered at 5 kHz and digitized at 20 kHz using NIDAQ data acquisition cards (National Instruments). Data acquisition was carried out using custom written-routines in MATLAB that also operated continuous video recording of the animal synchronized to the recording session. After 10-15 min of recording the juxtacellular pipette was advanced toward the cell and positive 200ms long current pulses (1-5nA) were delivered using a PG4000 Stimulator (Neurodata) so that the cell fired action potentials for 10-40 min.

**Immunohistochemistry, microscopy and image analysis on trans-synaptically labeled samples**

Series of 12-16 sections (each 480 μm apart) in the rostro-caudal axis of the brain were processed with standard fluorescent immunohistochemical techniques (double- and triple-labeling). For fluorescent immunocytochemistry, the following primary antibodies were used: chicken anti-GFP (GFP-1020; 1:1000, Aves), rabbit anti-dsRed (632496; 1:1000, Clontech), mouse anti-mCherry (632543; 1:1000, Clontech), mouse anti-Parvalbumin (P3088; 1:400, Sigma), or rabbit anti-Somatostatin (T-4103; SOM; 1:500, Peninsula Labs). Secondary antibodies (Alexa Fluor, 1:400 dilution, Invitrogen) used were: goat anti-chicken 488 (A11039), anti-rabbit 594 (A11037) or 647 (A21244), and anti-mouse 594 (A11032) or 647(A21236). Nuclear counterstain was performed using bisbenzimide.

Images were acquired using a Leica TCS SP5X upright confocal microscope. For analysis of double-labeling for mCh and PV or SOM, images were acquired with a 20x objective at 1.0x optical zoom and 2 μm step size through the z-plane with the pinhole set at 1 Airy unit. Images were imported into Adobe Photoshop CS6 and analyzed for co-localization of immunoreactivity. Quantification was performed on sections spaced 480 μm apart that spanned the rostral-caudal extent of each hippocampus. Within the DG, CA3 and CA1, identification of PV[+] and SOM[+] interneurons was based on morphology, location and marker labeling. Cells that were both mCh[+] and marker[+] but GFP[-] were counted. The data for each region were then divided by the total number of mCh[+]/marker^{+} cells summed from all three regions.

**Neuronal identification and antibody staining after juxtacellular labeling**

Experiments were terminated and the mice were perfused transcardially within two hours. The mice were placed under deep anesthesia using a ketamine/xylazine cocktail and were perfused using saline followed by a fixative containing 4% PFA and 0.2% picric acid dissolved in 0.1 M phosphate buffer (PB). Following overnight fixation, the brains were sectioned using a Vibratome (Leica VT1200). Sections were first incubated in Alexa 594- or 488-conjugated streptavidin (1:1000, Molecular Probes) then sections containing the labelled cell were selected for further immunohistochemical analysis. The following primary antibodies were used: rabbit anti-parvalbumin (PV27; 1:2500; Swant, Switzerland); rat anti-somatostatin (MAB354; 1:1000; Millipore, Temecula, CA); rabbit anti-neuronal nitric oxide synthase (160870; 1:1000; Cayman Chemical, MI); guinea pig anti-cannabinoid receptor type1 (CB1-6P-Af530; 1:1000; Frontier Science Co., Ltd, Japan); rat anti-muscarinic acetylcholine receptor type 2

(MAB354; 1:1000; Millipore, Temecula, CA); rabbit anti calbindin (CB38; 1:1000; Swant, Switzerland), mouse anti ankyrin-G (sc12719; 1:100; Santa Cruz Biotechnology, CA). Primary antibodies were diluted in 0.1 M PB containing 0.25% Triton X100 and sections were incubated overnight at 4°C in the antibody cocktails. Ankyrin-G staining was preceded by incubating sections in 0.2 mg/ml pepsin (S3002; Dako) in 0.2 M HCl for 5 min (Szabó et al., 2010). Primary antibodies were detected using secondary antibodies raised in goat against rabbit/rat/guinea pig/mouse conjugated to Alexa 488/594 (11005, 11008, 11007, 11001, 11076, 11006; Invitrogen) or raised in donkey against rabbit and conjugated to Alexa 647 (711-605-152; Jackson Laboratories). Immunoreactivity was documented using a CCD camera attached to a Zeiss Axioscope microscope or a Zeiss LSM 710 confocal microscope. After the immunochemical characterization, the labelled cells were visualized by 3,3'-diaminobenzidine tetrahydrochloride (DAB) and reconstructed in 2D based on Z-stack images taken by a Zeiss microscope. Cells were identified based on their protein expression and/or targets. One axo-axonic cell was identified by detecting close appositions between the axo-axonic cell boutons and axon initial segments identified by ankyrin-G staining (Szabó et al., 2010). The other axo-axonic cell was identified by visual inspection based on the unequivocal presence of the characteristic candelabra-like rows of boutons.

**Analysis of electrophysiological data**

For SWR detection, the LFP was filtered between 90-200 Hz. The program examined the envelope on the absolute values of the signals, and when the envelope crossed the threshold of 5 standard deviations, the event was considered a SWR. The start and end points of SWRs were specified as the time points where the signal reached a threshold of 2 standard deviations. All detected SWR events were inspected manually and artifacts were discarded.

To determine if a cell was modulated by SWRs or the action potentials during SWRs arose by chance, two different statistical simulations were performed. First, the time of occurrence of all recorded action potentials were pseudo randomly distributed 1000 times and the number of spikes that fell within SWRs was calculated for each simulation. These numbers were then sorted from highest to lowest. The P-value was calculated by determining where the number of spikes occurring during SWRs in the actual recordings ranked within the sorted simulated spike numbers. Firing modulation by SWR was considered significant if the number of spikes occurring during SWRs was greater than the highest 95% of the simulation results. Second, another set of simulations was performed where the temporal structure of the spike trains was preserved; here, instead of randomizing the spike train, the LFP trace was circularly shifted by a random interval of time 1000 times, so that the relative timing between the SWR episodes was preserved but the timing of spikes relative to the SWRs was shifted. Then we again determined the number of spikes falling within the relocated SWR events. Again, SWR modulation was considered significant if the number of spikes occurring during simulated SWRs was higher than the highest 95% of the simulation results. A cell was considered SWR-modulated if the end result of both simulations was significant. Additionally, spike rate plots for each cell triggered by SWR center were visually inspected for verification.

Dentate spikes were recorded during rest by the juxtacellular electrode in cases where interneurons were located within or close to the hilus (3 DG fast-spiking basket cells and 5 hilar dendrite targeting neurons). Both type 1 and type 2 dendritic spikes (Bragin et al., 1995) could be observed, but they were pooled together for the purposes of the present investigation, as done in other studies (Headley et al., 2016; Penttonen et al., 1997). To detect dendritic spikes, an automated approach was used based on a pattern-recognizing software function. First, in the actual recording, one event was selected that clearly met the criteria of being a dendritic spike, i.e., <50ms field potentials with at least twice the amplitude of the "background" LFP (Bragin et al., 1995; Penttonen et al., 1997). The program then used this single event as a template to find all the similar events in the recording. All matches were then manually inspected and the artefacts and events not meeting the above criteria were discarded.

For comparisons of firing rates inside and outside dendritic spikes, and for the time course analysis of SWR-related modulation, the spiking rate was calculated using a 50ms-long sliding window. Care was taken to prevent the generation of artificial patterns for SWRs co-occurring within the same time window. Specifically, raster plots and spiking rates were regenerated for each cell, and spikes corresponding to SWRs that co-occurred within a variable time window were rejected. As these regenerated raster and spiking rate plots resulted in very similar patterns, the non-rejected versions were used for analysis and display purposes, with the exception of one fast-spiking basket cell where the SWRs occurred at a particularly high frequency (600 SWRs/500s) – in the latter case, the co-occurring SWRs within 500ms were rejected. Another possible concern is the disruption of the natural timing pattern of SWR occurrence by splitting the recordings to "run" and "rest" parts. To test the effect of this factor, the raster and spiking rate plots were recalculated using the intact recordings for each cell. These regenerated plots were virtually identical to the ones generated by recording portions categorized as "rest" (not shown).

Traces used for the analysis of recordings made during juxtacellular labeling ranged from 460s to 850s in length. First, action potential (ch1) and SWR times of occurrence (ch2) were determined for the entire trace. Then, positive and negative voltage artefacts were detected to find the beginning and end of current injection. An action potential histogram was then plotted for the 200ms long window by aligning each window with the SWRs centered in the middle. Finally, the spiking rate was plotted by using a 20ms long sliding window on the histogram. As the spiking frequency varies and the injected current has to be constantly adjusted during labeling, to avoid including incidents when the cell did not spike (due to low current) and incidents when the cell spiked excessively (due to too high current), windows containing at least 1 action potential and less than or equal to 100 action potentials were selected. Repeating this analysis with different spike number ranges (1-50; 5-100) resulted very similar spiking rate plots.